

String Formation and Arrested Ordering Kinetics in Nematics Induced by Polar Particles

Pawan Kumar Mishra^{a,1,*}, Partha Sarathi Mondal^{a,1}, Pratikshya Jena,¹ and Shradha Mishra¹

¹Indian Institute of Technology (BHU), Varanasi, 221005, India

(Dated: February 24, 2025)

Our study explores the mixture of polar particles in apolar environment. We employ a coarse-grained approach to model the mixture, where polar particles are in minority. The interaction between polar and apolar components is incorporated via a coupling term in the free energy. Coupling generates local interaction in the system which results in the formation of string like structures connecting a pair of half integer topological defects. The increase in the coupling strength or the density of polar particles results in the: Sharper strings with larger probability of connecting the topological defects of same charge and the enhanced dynamics of topological defects. However, the ordering kinetics of the system shows the delayed coarsening for larger coupling or polar density. Our results can be used to develop controlled kinetics as well as to detect the impurities in liquid crystals.

Polar-apolar mixtures, in which one component exhibits polar symmetry (e.g., fish, bacteria, molecular motors, or certain types of synthetic rods) and the other shows nematic or apolar symmetry (e.g., liquid crystals), are common in both biological and synthetic systems [1–3]. When polar particles are introduced into a nematic liquid crystal environment, fascinating collective behaviors and complex defect dynamics can emerge due to interactions between the polar and apolar phases. Liquid crystals are particularly known for their ability to host topological defects in nematics. In these nematic liquid crystals, topological defects carry charges of $\pm\frac{1}{2}$ and move diffusively, eventually annihilating as the system relaxes toward equilibrium [4, 5]. Remarkably, this defect behavior persists even when the system is active—where the medium consists of self-driven units leading to the concept of “active nematics” [6–12].

The inclusion of foreign particles can significantly alter the dynamics of both active and passive nematic systems. Several studies have examined the effects of bacteria and other inclusions in liquid crystal environments, uncovering the formation of unique structures and dynamics that are absent in pure systems [13–21]. In this work, we investigate the general case of a polar-apolar mixture, employing a coarse-grained approach to study the interactions between a nematic liquid crystal and dilute polar particles. This framework enables us to understand how passive polar particles affect the structure and dynamics of nematic like topological defects and ordering kinetics within the apolar liquid crystal. This makes our study different from the previous spin-based models, where polar and nematic interactions coexist [22–24], but in our approach, we treat polar and apolar particles as distinct components interacting via a coupling term.

In this letter we introduce a mixed system of apolar and polar particles, where polar particles are less in

number. The system is modeled using the time Dependent Ginzburg-Landau (TDGL) equations for the local order parameters for polar and apolar particles, which is obtained by the variation of a combined free energy functional of pure polar, apolar and coupling term. The strength of coupling and density of polar particles are the two key control parameters in the system. Both parameters can be tune in the experiments by tuning the flexibility and density of polar particles.

We study the mixture by assuming external polar particles to be passive and present in small numbers, e.g., a few polar particles present in the liquid crystal. In this framework, the steady state of the pure polar system is disordered, and the average density of the apolar particles is chosen in such a way that its steady state is ordered in the absence of polar particles.

We focus our study on the behavior of topological defects formed in the liquid crystal during the evolution of the system starting from the disordered configuration of both apolar and polar particles. The relative strength of the two types of interaction dictates the kinetics and steady state behaviour of the system. When quenched from the random disordered state for both types of particles, the apolar particles try to form the ordered domains and polar particles prefer the disordered state, but the coupling works as a communicating medium between the two types of particles.

We found that for the small coupling strength, the interaction is weak and the mixture behaves like pure polar and apolar systems: (i) After a threshold value of coupling the interaction starts to dominate and string type structures are formed connecting the two-topological defects of same or opposite charges; (ii) The structure of the strings sharpens and the probability of connecting the two ends of the strings with the topological defects of the same charge increases and (iii) The dynamic of the two types of defects increases with coupling and density of polar particles. Additionally the ordering kinetics get arrested due to interaction with the defects of the same charges.

Model:- We consider a system where few polar particles are immersed in the liquid crystal. We model the system using coarse-grained free energy functional for the indi-

* pawankumarmishra.rs.phy19@itbhu.ac.in; Current affiliation: Mechanobiology Institute, National University of Singapore, 117411 Singapore

^a These authors contributed equally to this work

vidual systems and then introduced a coupling between polar and apolar particles. For polar particles, the orientation order parameter is represented by the polarization vector field $\mathbf{P} = (P_x, P_y)$, while for apolar (nematic) particles, it is given by the tensor order parameter \mathbf{Q} , which is a 2×2 tensor with two-independent components Q_{xx} and Q_{yy} in two-dimensions., where x and y are the cartesian space directions.

The free energy functional F_Ψ for individual system is the Landau-Ginzburg Free energy functional given by:

$$F_\Psi = \int d\vec{r} \left[\frac{\alpha_\Psi(\rho_0)}{2} \Psi^2 + \frac{\beta_\Psi}{4} \Psi^4 + \frac{\kappa_\Psi}{2} (\nabla \Psi)^2 \right] \quad (1)$$

where Ψ represents the order parameters of the system. $\Psi = \mathbf{P}$ and \mathbf{Q} for the polar and nematic fields respectively. $\Psi^2 = \mathbf{P} \cdot \mathbf{P}$ and $\mathbf{Q} : \mathbf{Q}$, $\Psi^4 = (\mathbf{P} \cdot \mathbf{P})^2$ and $(\mathbf{Q} : \mathbf{Q})^2$. $(\nabla \Psi)^2 = (\nabla \mathbf{P}) : (\nabla \mathbf{P})$ and $(\nabla \cdot \mathbf{Q}) \cdot (\nabla \cdot \mathbf{Q})$. The tensor scalar product for two tensors A and B is given by $A : B = A_{lk} B_{kl}$ and the scalar product of a vector with a tensor $\vec{C} \cdot A = C_j A_{ji}$. The coefficient $\alpha_\Psi(\rho_0)$ is responsible for the order-disorder transition and is given by: $\alpha_\Psi(\rho_0) = \alpha_0 \left(1 - \frac{\rho_0}{\rho_c} \right)$, where ρ_c is the critical density, ρ_0 is the average density of either polar (ρ_{p_0}) or apolar (ρ_{a_0}) particles, and α_0 is a constant. The system is in the homogeneous ordered phase for $\alpha_\Psi < 0$ and in the disordered phase for $\alpha_\Psi > 0$. The coefficient $\beta_\Psi > 0$ ensures the stability of the system. The third term accounts for the elastic distortion in the \mathbf{P} or \mathbf{Q} fields in the equal elastic constant limit [4]. Here, κ_Ψ are the elastic constants, and for convenience, we take $\kappa_\Psi = \kappa = 1$ and $\beta_\Psi = \beta = 1$ for both the fields.

Due to the interaction between the two types of particles, they prefer to align along the long axis of each other. Thus, we introduce a coupling term of the form $(\mathbf{Q} : \mathbf{P}\mathbf{P})$ in the free energy of the mixed system. The total free energy of the system is

$$F_m = F_P + F_Q + \gamma \int (\mathbf{Q} : \mathbf{P}\mathbf{P}) dr, \quad (2)$$

γ is the coefficient of the coupling between two types of fields and it is relevant parameter in the model. For $\gamma = 0$, the two fields are uncoupled.

The evolution of the order parameters \mathbf{P} and \mathbf{Q} is governed by a generalized dynamical equation derived from variation of the free energy functional F_m with additional thermal fluctuations introduced through the stochastic noise term. The equations for the two fields \mathbf{P} and \mathbf{Q} are:

$$\frac{\partial \mathbf{P}}{\partial t} = [\alpha_P - \beta_P |\mathbf{P}|^2] \mathbf{P} + \kappa_P \nabla^2 \mathbf{P} + \gamma (\mathbf{P} \cdot \mathbf{Q}) + \zeta_P(\mathbf{r}, t) \quad (3)$$

where, $|\mathbf{P}|^2 = P_x^2 + P_y^2$ and

$$\begin{aligned} \frac{\partial Q_{ij}}{\partial t} &= [\alpha_Q - \beta_Q (\mathbf{Q} : \mathbf{Q})] Q_{ij} + \kappa_Q \nabla^2 Q_{ij} \\ &+ \gamma (P_i P_j - \frac{1}{d} \delta_{ij} |\mathbf{P}|^2) + \zeta_Q(\mathbf{r}, t) \end{aligned} \quad (4)$$

Here, ζ_P, ζ_Q are the Gaussian white noise terms representing the thermal fluctuations. The noise satisfies the properties $\langle \zeta_\Psi \rangle = 0$ and $\langle \zeta_\Psi(r, t) \zeta_\Psi(r', t') \rangle = \eta_\Psi \delta(r - r') \delta(t - t')$, where $\eta_\Psi = \eta$ is the noise strength for both the fields.

We study the system in two dimensions. The dynamics of both the polarization \mathbf{P} and the tensorial order parameter \mathbf{Q} are analyzed. The intrinsic time $\tau = \frac{1}{\alpha_0} = 1$ and length $l_0 = \sqrt{\kappa\tau}$ scales are used to rescale the system. The equations are made dimensionless using τ and l_0 . The details of numerical simulation are provided in Sec.1 in Appendix.A.

The system is initialized from a randomized and homogeneous state of apolar particles with an average apolar density $\rho_{a_0} = 0.75$, and critical densities $\rho_{pc} = \rho_{qc} = 0.5$. The value of ρ_{a_0} is chosen such that the apolar particles are in the ordered phase. The strength of the noise η is set to 0.1. The average density of polar particles ρ_{p_0} and the coupling strength γ are the primary control parameters in the study. ρ_{p_0} is varied to ensure $\rho_{p_0} \ll \rho_{pc}$, keeping the pure polar particles in the disordered phase, while γ is varied in the range $[0, 1]$. The focus of our study is different from the other coupled polar-apolar mixtures, where the density of both types of particles are comparable [13, 25] as well as the systems are studied in confinement [26].

Results:- In this study, we examine how coupling influences the structure formation and dynamics within the system. Our focus lies in observing the time evolution of the nematic order parameter field \mathbf{Q} , and the polarization vector field \mathbf{P} as governed by Eq. (4) and (3). The kinetics of the system very much depends on the formation of oppositely charged disclinations, which are topological defects of charge half-integer and integer in pure apolar and polar systems respectively.

Strings in the system: We begin by illustrating the effect of coupling on both polar and nematic fields through snapshots in FIG.1. Panels (a) and (b) show the \mathbf{Q} -field, for $\gamma = 0$ and $\gamma = 1$, respectively, while panel (c) displays the \mathbf{P} -field. The color represents the magnitude of two fields in respective snapshots and lines are the stream lines showing the local orientation in the system. At zero coupling ($\gamma = 0$), the polar species remains disordered, and the nematic system exhibits typical behavior for liquid crystals: the \mathbf{Q} -field exhibits half-integer defects which diffuse freely and annihilate upon colliding with opposite-charge defects. As the coupling is turned on, the polar species begin to align and the direction of local polar ordering is influenced by the local nematic ordering and *vice versa*. At a finite γ , small domains of \mathbf{P} -field start forming and on further increase in coupling strength, new structures, which we call 'strings', in \mathbf{Q} and \mathbf{P} fields appear in the system, connecting two topological defects.

For the nematic species, the magnitude of \mathbf{Q} along the string is significantly less than that in the surrounding regions, as shown in FIG.1(b). Similar string-like structures connecting two half-integer topological defects have been reported in recent experimental [27] and theoretical [25, 26] studies. However, unlike these works, the strings

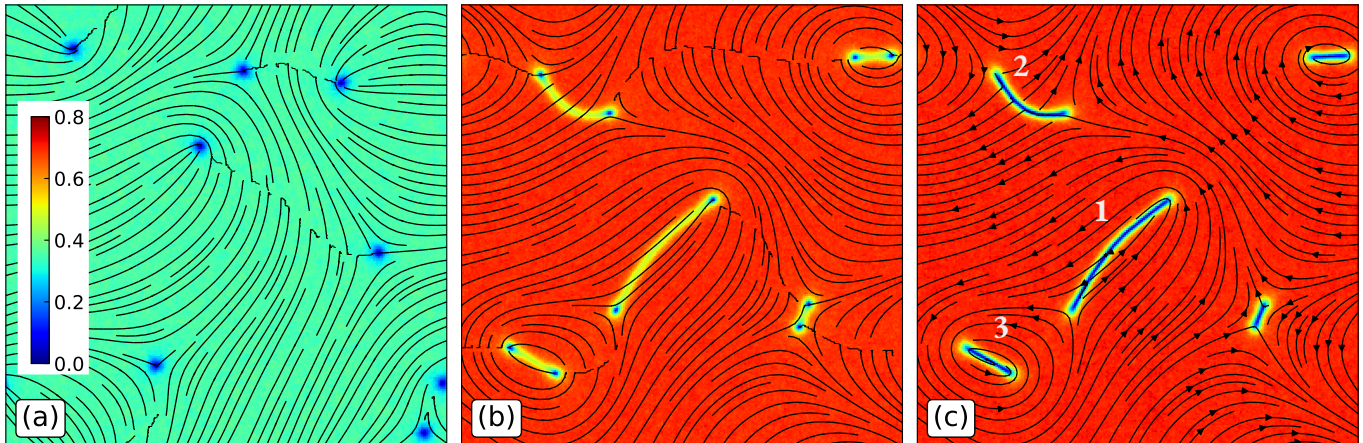


FIG. 1. Visualization of order parameters. Panels (a) and (b) illustrate the \mathbf{Q} field for $\gamma = 0$ and $\gamma = 1.0$, respectively, while panel (c) depicts the \mathbf{P} field for $\gamma = 1.0$. The streamlines indicate the direction of the corresponding order parameter fields, and the color bar represents their magnitudes.

in our case are observed to connect defects of both the same (e.g., two $+\frac{1}{2}$ or two $-\frac{1}{2}$ as marked by ‘2’ and ‘3’ in FIG.1(c)) as well as of opposite types (e.g., a $+\frac{1}{2}$ and a $-\frac{1}{2}$ as marked by ‘1’ in FIG.1c)). The magnitude of \mathbf{P} i.e. $|\mathbf{P}| = (\mathbf{P}x^2 + \mathbf{P}y^2)$ approaches 0 along the string with the opposite orientation of \mathbf{P} -field on its two sides, as shown in FIG.1(c). This indicates that the strings act as domain walls between two polar domains with opposite orientations and both fields (\mathbf{Q} and \mathbf{P}) shows the nearly parallel or perpendicular anchoring along the string as shown by the strings labeled as ‘1’ and ‘2’ respectively in Fig.1(c). We also checked the effect of large density of polar particles ρ_{p0} or high coupling γ . For large coupling $\gamma > 1$ and high density $\rho_{p0} \sim 0.4$, the magnitude of local ordering increases and strings are more probable to be formed between a pair of 1/2-integer defects of same charge. But even for high coupling and large density we never found integer defects in the system. The snapshots of the \mathbf{Q} and \mathbf{P} is shown in FIG.S2 in Sec.3 in Appendix.A.

Starting from a random state, it takes sometime for the defects to appear and the strings to form. After this initial state, the width of the strings remains the same as long as the defects survive, which we refer as dynamical steady state. The presence of strings introduces complexity into the system’s dynamics, as their configuration evolves with the motion of defects. The annihilation of defects can either lead to the disappearance of existing strings or the formation of the new ones. The animations showing the time evolution of \mathbf{Q} and \mathbf{P} field provided in Sec.6 in Appendix.A.

The range of γ values for which the strings are formed depends strongly on the mean density of the polar species (ρ_{p0}). This dependence is visually represented by a series of snapshots provided in FIG.S1 in Appendix.A. For larger ρ_{p0} , the string formation is observed at relatively lower coupling strengths. We also calculate the normalised width W_b of the strings. The details of calculation of width are presented in Sec.2 in the Appendix.A. The result obtained for the magnitude of W_b is presented in the form of a phase diagram in FIG.2(a) in the $(\rho_{p0} - \gamma)$

plane. We again show W_b vs. γ for three different densities ρ_{p0} in FIG.2(e). Higher densities of polar particles and stronger coupling strengths lead to narrower strings.

The mechanism of formation of the strings involves the interplay of the two length scales : $\xi_P = \sqrt{\frac{1}{\alpha_{P0}}}$, which governs the variation of the polarization modulus, and $\xi = \frac{1}{\gamma}$, which controls the variation of the polarization direction under the assumption of a constant nematic field. In practice, the larger of these two length scales dominates. To delve deeper into the interplay of two length scales, we switch off the noise and study geometries with rigid boundary condition in one direction which can generate a wall. We introduced two rigid walls at the top and bottom, where the \mathbf{Q} -field is fixed with perpendicular anchoring at the two walls and \mathbf{P} -field also perpendicular anchoring with opposite orientations at the top and bottom walls. The \mathbf{Q} -field inside the geometry is kept homogeneously ordered matching with the walls and \mathbf{P} is random. The periodic boundary condition is used in x -direction and width of the system D is much smaller than its length L . For the regime where $\xi_P, \xi > D$, no wall is observed. However, when $\xi_P, \xi < D$, a wall forms. For this geometry and boundary conditions the steady state has stable wall in the middle of the system ($y = D/2$). In Fig.2(b-d) we show the snapshot of the system with magnitude of local \mathbf{P} and its direction at the two boundaries for three different γ values, $\gamma = 0, 0.6, 1.0$, at a fixed ρ_{p0} for system dimensions $D = 20l_0$, and $L = 100l_0$. We quantify the width of the wall, W , by counting the number of sites where the magnitude of the polar order parameter satisfies $|\mathbf{P}| < 0.2$ along the y -directions and averaged over x -direction at the dynamical steady state. In FIG.2(f) we show the plot of relative width of the wall $W_c = W/D$ vs. γ for three different ρ_{p0} . Both by increasing γ and ρ_{p0} , W_c monotonically decreases for confined system which is consistent with the plot shown in FIG.2(e) for the bulk system.

Kinetics of the system: Now we shift our focus to examine the effect of coupling on the ordering kinetics of \mathbf{Q} -field. Starting from a random homogeneous state, the

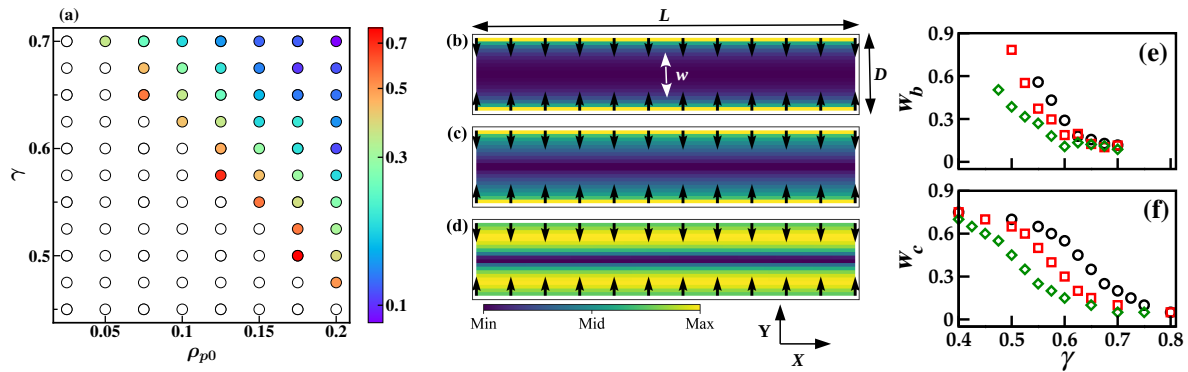


FIG. 2. (a) Phase diagram illustrates the width of strings W_b (color map) in the $(\rho_{p_0}-\gamma)$ plane. The empty symbols indicate the values of ρ_{p_0} and γ where strings are absent. (b)-(d) Snapshots of the \mathbf{P} field for $\gamma = 0, 0.6,$ and 1.0 in a confined system with perpendicular anchoring of \mathbf{P} field at the top and bottom boundaries. The color map represents the magnitude of \mathbf{P} field. (e) Plot of W_b versus γ for three values of $\rho_{p_0} = 0.15, 0.175,$ and 0.20 represented by \circ, \square and \diamond respectively. (f) Plot of $W_c = \frac{W}{D}$ versus γ for three values of the ρ_{p_0} is the same as in plot (e).

system evolves through the growth of ordered domains of nematic field. To characterize the domain growth, we calculate the correlation length $L(t)$ from the 0.5 crossing of the two-point correlation function, $C(r, t)$ (see Sec.4 in the Appendix.A). For all values of γ , $L(t)$ overlaps at initial times. At intermediate times, the $L(t)$ vs t plot exhibits a plateau for $\gamma \geq 0.6$, whereas at late times, the behavior is consistent with $t^{1/2}$ for all γ , with the magnitude of $L(t)$ strongly dependent on γ .

During the initial times, the nematic system starts growing from random initial conditions, and small domains of \mathbf{Q} begin to emerge. Hence, the growth of $L(t)$ in this regime is independent of γ , leading to the overlapping curves. At intermediate times, the strings are absent for $\gamma \leq 0.5$, and $L(t)$ matches well with the pure system. For $\gamma \geq 0.6$, the system reaches a dynamical steady state, and the presence of strings affects the growth of $L(t)$, resulting in the plateau observed during the intermediate times. The appearance of the plateau signifies arrested coarsening during intermediate times. The plateau region consistently flattens with increasing γ , while the length of the plateau region shows non-monotonic behavior: it first increases for $0.6 \leq \gamma \leq 0.8$ and then decreases for $\gamma \geq 0.8$.

At higher γ ($\gamma \gtrsim 0.6$), the effect of coupling on the dynamics of the \mathbf{Q} -field is two-fold: (i) Increasing coupling leads to the enhancement of the probability of formation of strings connecting defects of the same type, denoted by P_s ; (ii) The dynamics of an isolated defect increases with increasing coupling strength. In FIG.3(b), we show the plot of P_s versus γ for three different densities ρ_{p_0} . The probability P_s increases monotonically with γ and ρ_{p_0} , i.e., with increasing coupling strength, the strings are more likely to connect defects of the same sign. On the other hand, to understand the effect of coupling strength on the dynamics of defect, we introduce a pair of artificial half-integer topological defects in the system and its details are presented in Sec.5 in the Appendix.A. As shown in

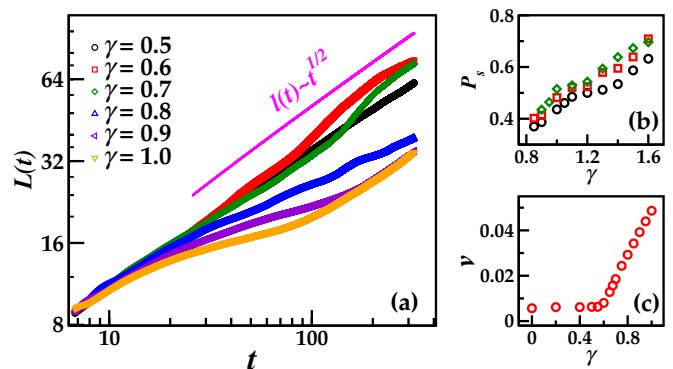


FIG. 3. (a) Correlation length $L(t)$ vs. t for various γ for $L = 1024$ and $\rho_{p_0} = 0.1$. (b) The probability P_s vs. γ for different $\rho_{p_0} = 0.05, 0.10$ and 0.15 represented by \circ, \square and \diamond respectively for $L = 256$. (c) Speed of the isolated half integer defects ($\pm 1/2$) v vs. γ .

FIG.3(c), the speed of defect remains unaffected upto $\gamma \approx 0.6$ in the absence of strings while it monotonically increases as strings appear in the system for $\gamma \gtrsim 0.6$.

We propose the mechanism behind the appearance of the plateau and its dependence on coupling through the interplay of two counteracting effects of coupling discussed above. Due to formation of strings connecting defects of same sign ($P_s \neq 0$), the annihilation of the defects of opposite charge are delayed which slows the growth resulting in the plateau in $L(t)$ during the intermediate time regime. With increase in γ , P_s increases which results in further flattening of $L(t)$ curve in the plateau region. In addition to that, increase in γ increases dynamic of isolated defects, which results in faster shrinking of strings as well as increased probability of collision of two defects of opposite charge as shown in FIG.S3 in the Appendix.A. This results in the decrease of the length of the plateau region for $\gamma \gtrsim 0.8$.

Conclusions:- We study the effect of polar impurities

in liquid crystal system by tuning the coupling strength γ and average density of polar particles ρ_{p_0} . We use the coupled time dependent Ginzburg Landau (TDGL) equations for order parameters \mathbf{Q} and \mathbf{P} . The coupling lead to the formation of string like structures in nematic order parameter field. The two end points of the strings are topological half integer defects. The strings are observed above some optimal value of coupling and density of polar particles. For polar particles, the magnitude of the order parameter is close to zero along the string, acting as a domain wall separating oppositely oriented domains. The strings are more probable to be connected by the defects of same sign for larger coupling and density, this results in delayed kinetics of domain formation for strong coupling. Opposite to this effect, the dynamics of single defects is enhanced by the strengthening of the string. These results highlight the dual role of $\mathbf{Q} - \mathbf{P}$ coupling in the system: while moderate coupling accelerates defect annihilation and promotes faster ordering, excessive coupling stabilizes same-type defect connections, ultimately hindering the ordering process. Additionally, increase in P_s with increase of γ leads to the formation of defect structures similar to ± 1 like topological charge formed by the very small string connecting the two $+1/2$ (or two $-1/2$) defects as shown in FIG.1(c) for $\gamma = 1$. This is counterintuitive since ± 1 charged defects are not stable topological structures for nematic.

In summary, this study provides a comprehensive analysis of the behavior of topological defects and string formation in coupled nematic and polar systems. The findings reveal the critical role of coupling strength and polar particle density in determining the structural and dynamical

properties of the liquid crystals with impurities. The strings we observed are analogous to the Dirac strings found in confined nematic liquid crystals [28]. However, our study suggests that these strings can also emerge dynamically as the system evolves toward an ordered state in the presence of polar particles.

Our results can be tested in experiments on apolar-polar mixture, where a few polar particles act like tiny magnets within the liquid crystals. In the current study the polar particles are passive in nature, the study can be further explored by introducing activity in polar particles.

ACKNOWLEDGMENTS

P.K.M. and S. M. thank Julia Yeomans for useful discussions. The authors thank Jacques Prost for useful suggestions, discussions and careful reading of the manuscript. P.K.M., P.S.M. gratefully acknowledge UGC for research fellowship and P.J. acknowledge the DST INSPIRE fellowship for funding this project. The support and the resources provided by PARAM Shivay Facility under the National Supercomputing Mission, Government of India at the Indian Institute of Technology, Varanasi are gratefully acknowledged by all authors. S.M. thanks DST-SERB India, ECR/2017/000659, CRG/2021/006945 and MTR/2021/000438 for financial support. P.K.M, P.S.M, P.J. and S.M. also thank the Centre for Computing and Information Services at IIT (BHU), Varanasi.

Appendix A: Supplementary Material

1. Simulation details

We have used the Euler integration scheme on a square lattice of size $L \times L$ with periodic boundary conditions in both directions. The Euler discretization scheme is applied with mesh sizes $\Delta x = \Delta y = 0.5l_0 = 0.5$ and time step $\Delta t = 0.01\tau = 0.01$. The spatial discretization ensures that coarsening interfaces are treated smoothly, while the temporal discretization is selected to maintain the stability of the numerical scheme. Once all grid points are updated, then it is counted as one simulation step. One simulation step covers Δt time. The results are obtained for system sizes 256×256 and 1024×1024 for time steps 1×10^5 and 3×10^5 respectively. For better statistics, the observable are averaged over 40 – 50 independent realizations. The parameters for the system with artificial defects and confined system are mentioned at respective locations.

2. Width calculation

We quantify the width of the structures connecting the topological defects shown in FIG.1(b) in the main text. To compute the width, we analyze the \mathbf{P} field in FIG.1(c) in the main text, which provides better contrast compared to the \mathbf{Q} -field. The width is determined by counting the number of sites, n_w , where the magnitude of the \mathbf{P} -field in FIG. S4 satisfies $|\mathbf{P}| < 0.2$ along both the X - and Y -directions, and then calculating the average of these values. To ensure accuracy, this averaging is performed across multiple locations in the system. Structures are considered as strings only if $n_w \leq 30$. To normalize the width, n_w is divided by 30, yielding the normalized width W_b . FIG. S4 presents a phase diagram showcasing snapshots of the \mathbf{P} -field, illustrating variations in string width as a function of different ρ_{p_0} and γ values.

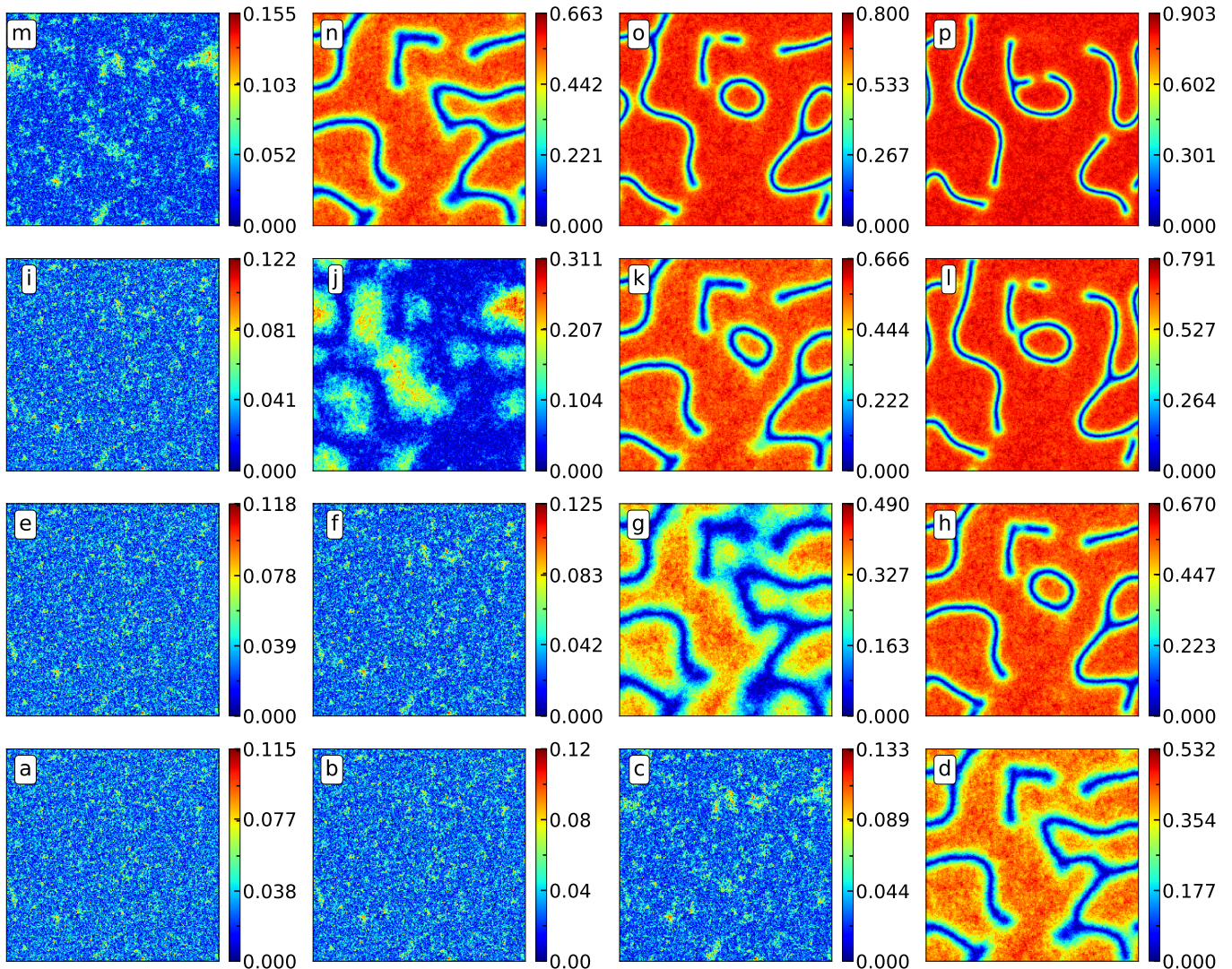


FIG. S4. Snapshot of the magnitude of polar order parameter at a fixed time, showing variations in the polar density ρ_{p_0} from left to right and the coupling strength γ from bottom to top. Each row (a-d, e-h, i-l and m-p) represents a different γ , varying from weak to strong coupling ($\gamma = 0.50, 0.55, 0.60, 0.65$) respectively. Each column (a-m, b-n, c-o and d-p) represents a different ρ_{p_0} varying from low to high (0.05, 0.10, 0.15, 0.20) respectively. The heatmaps in each row illustrate variations of the polar order parameter for the corresponding parameters.

3. Effect of higher coupling strength and high density

We also checked the results for high coupling $\gamma = 1.5$ and density $\rho_{p_0} = 0.4$. In FIG.S5 we show the local \mathbf{Q} and \mathbf{P} fields. Color bar and lines have the same meaning as in FIG.1 in the main text. For higher coupling the magnitude of local order parameters go beyond 1 due to the additional ordering effect of coupling γ . The animation of the same system can be found at Sec.A 6 in the supplementary material.

4. Kinetics of apolar order parameter

We define the two-point correlation function $C(r, t) = \langle \mathbf{Q}(\mathbf{r} + \mathbf{r}_0, t) : \mathbf{Q}(\mathbf{r}_0, t) \rangle$, where $\langle \dots \rangle$ denotes the isotropically averaged over different directions, and 50 independent runs. The system size taken into consideration is $K = 1024$. The Fig.S7(a-b) show the scaled correlation functions $C(r)$ vs. $r/L(t)$ for coupling strength $\gamma = 0.5, 1.0$ in sequence (main figure). The inset plots in (a-b) depict the time progression of the correlation functions $C(r)$ vs. r shown in different color from black ($t = 125$) to brown ($t = 2500$). For scaling, the characteristic length $L(t)$ is determined as the position where the correlation crosses 0.5. The correlation functions $C(r, t)$ display a good dynamical scaling for $\gamma = 0$ as well as 1.0. That implies the existence of single characteristic length scale $L(t)$ for the evolution for zero and

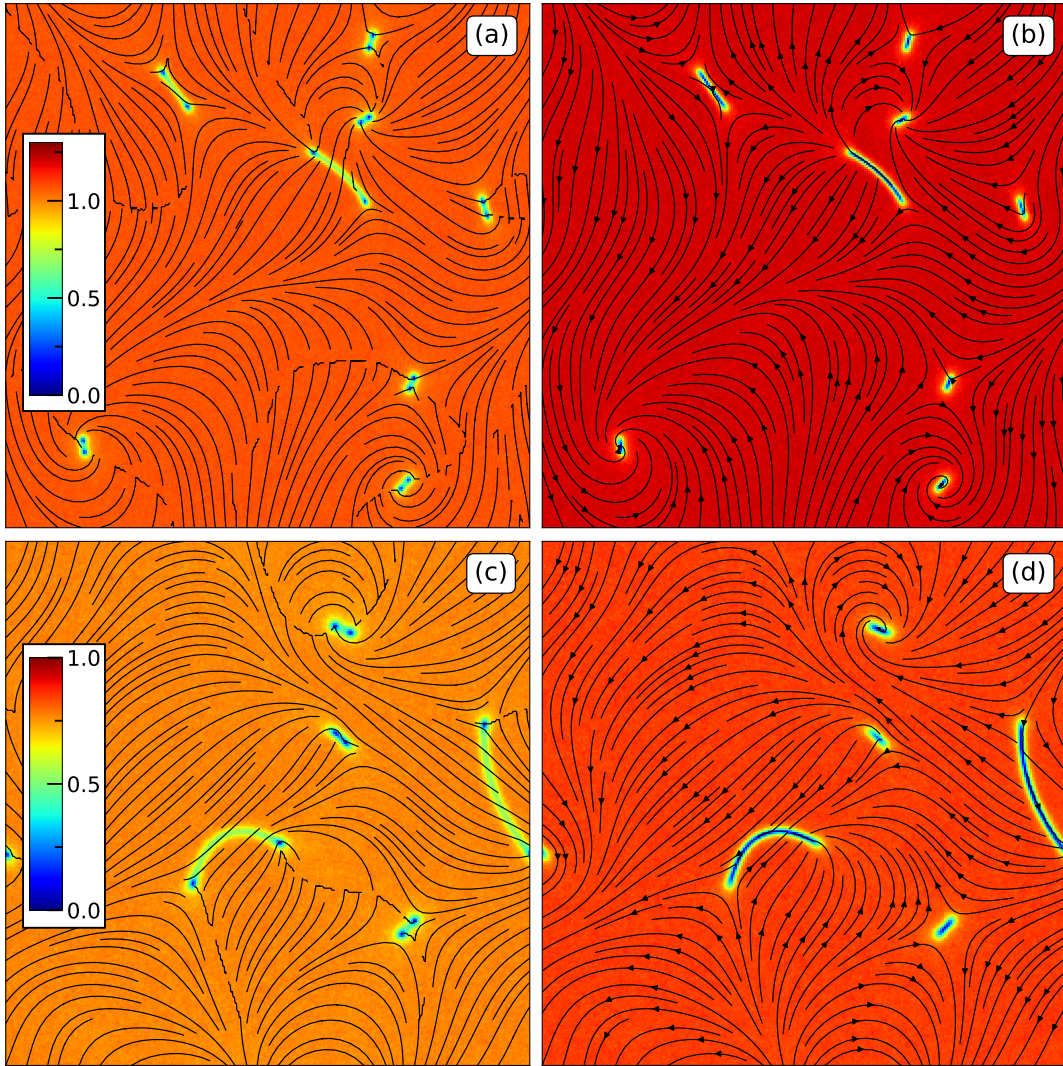


FIG. S5. The figure shows the snapshots of the system at high coupling in subplots (a-b) for $\gamma = 1.50, \rho_{p_0} = 0.20$ and at high density in subplots (c-d) for $\gamma = 1.00, \rho_{p_0} = 0.40$. Left column : snapshots of the apolar species where the color shows the magnitude of nematic order parameter, $|\mathbf{Q}|$, according to the color bar and the stream lines represent the orientation field of the apolar species. Right column : snapshots of the polar species where the color shows the magnitude of polar order parameter, $|\mathbf{P}|$, according to the color bar and the stream lines represent the orientation field of the polar species. Parameters : System size, $L = 256$, and rest of the parameters are same as in FIG.1 in the main text

finite coupling as well. But, surprisingly for intermediate coupling strength γ , we do not observe such scaling collapse (data not shown), That indicates the presence of multiple length scales in the system.

5. Artificial Defects in the Coupled System

The artificial defects are designed as: Let (x_1, y_1) and (x_2, y_2) are the location of defect cores, then the orientation of the nematic particles at position (x, y) is given by

$$\theta(\vec{r}) = \left[S \arctan\left(\frac{y - y_1}{x - x_1}\right) - S \arctan\left(\frac{y - y_2}{x - x_2}\right) \right] + \theta_0 \quad (\text{A1})$$

where, $\theta_0 = 0$ is the orientation far away from the defects such that nematic particles are aligned parallel to the horizontal axis and $S = \frac{1}{2}$ is the topological charge of the defect [29]. We chose $(x_1, y_1) \equiv (\frac{L}{4}, \frac{L}{2})$ and $(x_2, y_2) \equiv (\frac{3L}{4}, \frac{L}{2})$ and the orientation of the defects are chosen such that the head of the $+\frac{1}{2}$ defect is facing the $-\frac{1}{2}$ as shown in FIG. S8.

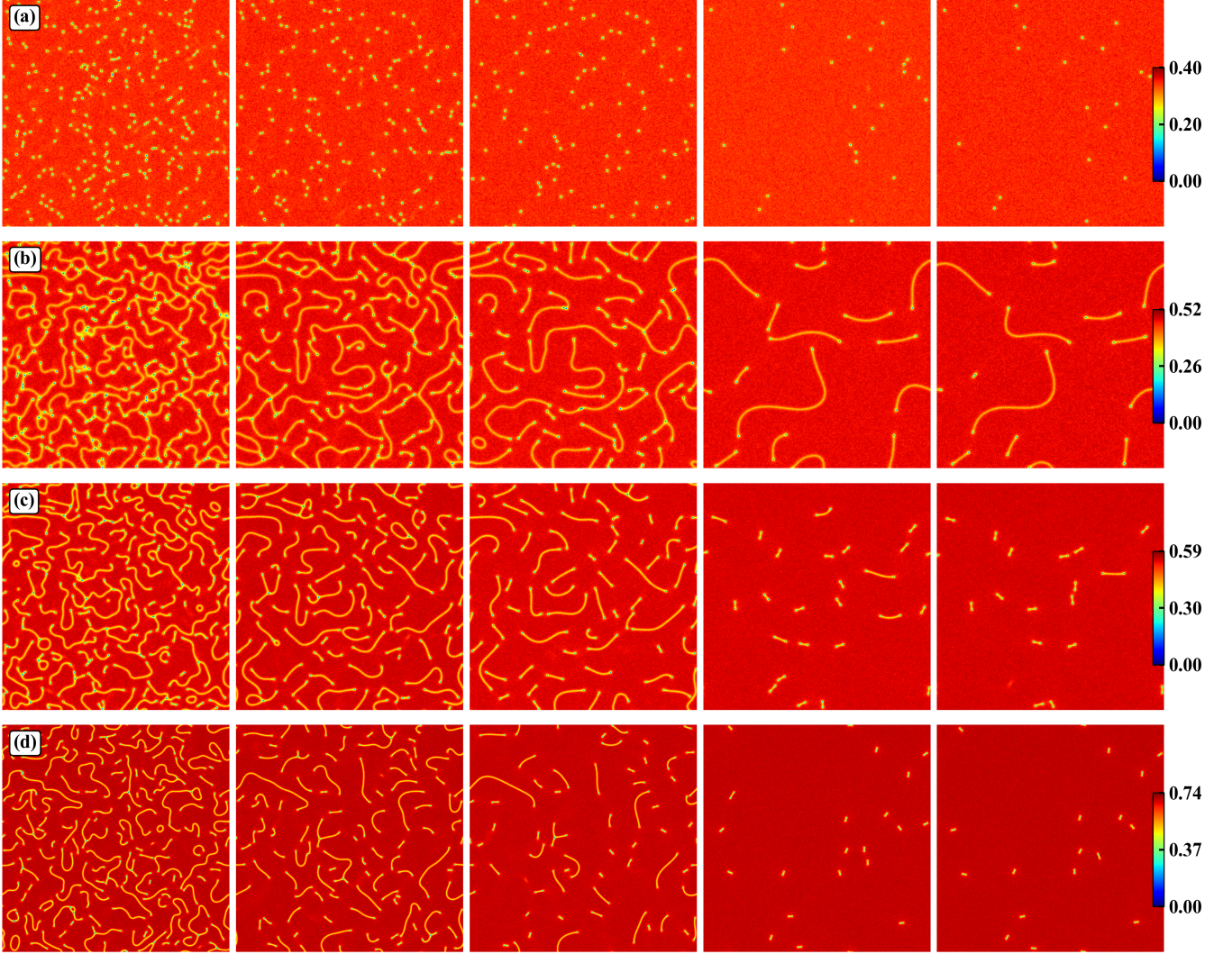


FIG. S6. The snapshots illustrate the time evolution of the Q -field across four panels (a-d), corresponding to coupling strengths $\gamma = 0, 0.7, 0.8, 1$, respectively. Each panel displays multiple figures, arranged from left to right, representing the evolution of Q -field over time at $t = 750, 1650, 3375, 6500, 16500, 21000$. The heatmap in each panel indicates the magnitude of the nematic order parameter for the corresponding system at that time.

Snapshots of the system with polar order initial condition are shown for $\gamma = 0$ and $\gamma = 1.0$. These snapshots provide insight into the initial configurations and the subsequent evolution of the system under different γ values.

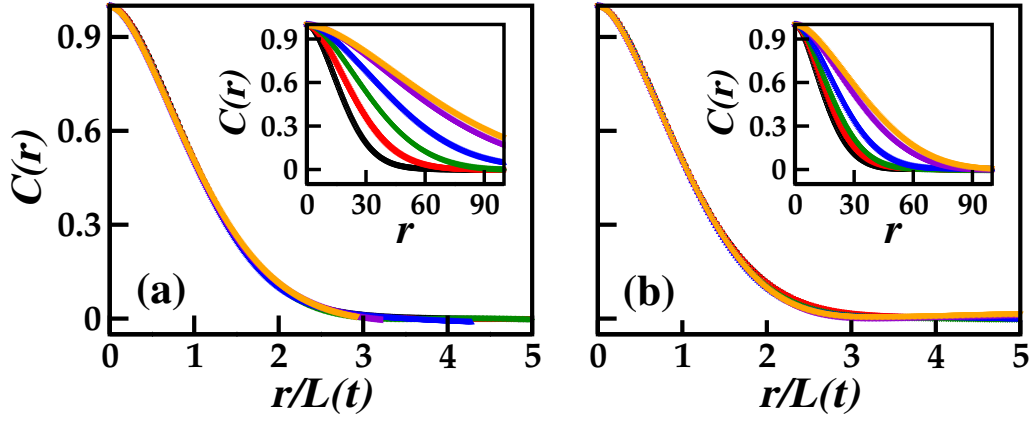


FIG. S7. Panels (a) and (b) display the scaled correlation functions $C(r)$ versus $r/L(t)$ for coupling strengths $\gamma = 0.5$ and $\gamma = 1.0$, respectively for $\rho_{p0} = 0.1$ in the main figures. The curves in both the main and inset figures represent the correlation functions at different time steps, with the color progression from black ($t = 125$) to brown ($t = 2500$) indicating the time evolution. The insets in panels (a) and (b) show the correlation functions $C(r)$ as a function of r .

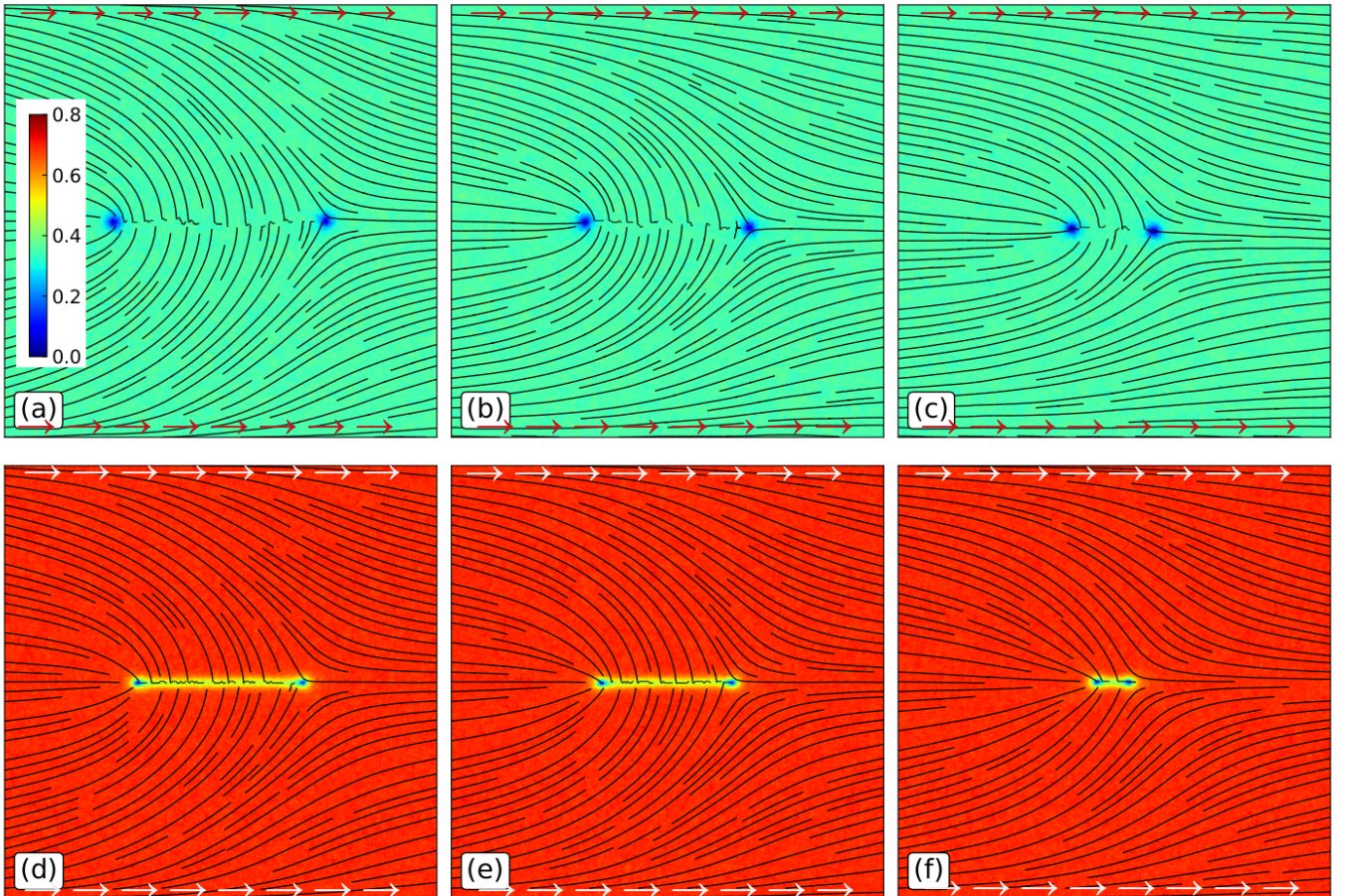


FIG. S8. Snapshots of the Q -field with artificial defects. (a-c) For $\gamma = 0$, snapshots are displayed at time $t = 30, 540$, and 1100 , respectively. (d-f) For $\gamma = 1.0$, snapshots are taken at time $t = 30, 60$, and 150 , respectively. The color map represents the magnitude of the Q -field, streamlines depict its orientation, and arrows along the boundary indicate the P -field.

6. Description of Supplementary Movies

Mov1 : The movie shows the evolution of the nematic order parameter field (\mathbf{Q}) for $\gamma = 0.0$, $\rho_{p0} = 0.20$. The colormap shows the magnitude of \mathbf{Q} and the headless arrows represent the orientation of the local nematic director.

Link : https://drive.google.com/file/d/1r7Y5IeG9q8QwL7jP5tIotpX1J_cedWw/view?usp=sharing

Mov2 : The movie shows the evolution of the nematic order parameter field (\mathbf{Q}) for $\gamma = 0.70$, $\rho_{p0} = 0.20$. The colormap shows the magnitude of \mathbf{Q} and the headless arrows represent the orientation of the local nematic director.

Link : <https://drive.google.com/file/d/1Lt3JF1ml3pw957CAeuoElqJ-Pt338d4i/view?usp=sharing>

Mov3 : The movie shows the evolution of the polar order parameter (\mathbf{P}) for $\gamma = 0.70$, $\rho_{p0} = 0.20$. The colormap shows the local magnitude of \mathbf{P} and the arrows represent the local orientation of \mathbf{P} .

Link : https://drive.google.com/file/d/1rK_UUUuAxk2LqWEI_eLjRT05QirQsQJd/view?usp=sharing

Mov4 : The movie shows the evolution of the nematic order parameter field at high mean density of polar species ($\rho_{p0} = 0.30$) for $\gamma = 1$. The colormap shows the local magnitude of \mathbf{P} and the arrows represent the local orientation of \mathbf{P} .

Link : https://drive.google.com/file/d/1a8V6Pe_c_g9pHWA3qJKujTsSygyFMVnb/view?usp=sharing

-
- [1] R. R. Trivedi, R. Maeda, N. L. Abbott, S. E. Spagnolie, and D. B. Weibel, Bacterial transport of colloids in liquid crystalline environments, *Soft Matter* **11**, 8404 (2015).
 - [2] Y. Sasaki, Y. Takikawa, V. S. Jampani, H. Hoshikawa, T. Seto, C. Bahr, S. Herminghaus, Y. Hidaka, and H. Orihara, Colloidal caterpillars for cargo transportation, *Soft matter* **10**, 8813 (2014).
 - [3] S. Tatarkova, D. Burnham, A. Kirby, G. Love, and E. Terentjev, Colloidal interactions and transport in nematic liquid crystals, *Physical review letters* **98**, 157801 (2007).
 - [4] *The physics of liquid crystals*, 83 (Oxford university press, 1993).
 - [5] S. Chandrasekhar, *Liquid Crystals*, 2nd ed. (Cambridge University Press, 1992).
 - [6] S. Mishra, S. Puri, and S. Ramaswamy, Aspects of the density field in an active nematic, *Philosophical Transactions of the Royal Society A: Mathematical, Physical and Engineering Sciences* **372**, 20130364 (2014).
 - [7] S. Mishra, Giant number fluctuation in the collection of active apolar particles: From spheres to long rods, *Journal of Statistical Mechanics: Theory and Experiment* **2014**, P07013 (2014).
 - [8] S. Kumar and S. Mishra, Active nematics with quenched disorder, *Physical Review E* **102**, 052609 (2020).
 - [9] A. Doostmohammadi, J. Ignés-Mullol, J. M. Yeomans, and F. Sagués, Active nematics, *Nature communications* **9**, 3246 (2018).
 - [10] L. Giomi, M. J. Bowick, P. Mishra, R. Sknepnek, and M. Cristina Marchetti, Defect dynamics in active nematics, *Philosophical Transactions of the Royal Society A: Mathematical, Physical and Engineering Sciences* **372**, 20130365 (2014).
 - [11] S. Thampi and J. Yeomans, Active turbulence in active nematics, *The European Physical Journal Special Topics* **225**, 651 (2016).
 - [12] S. P. Thampi, R. Golestanian, and J. M. Yeomans, Instabilities and topological defects in active nematics, *Europhysics Letters* **105**, 18001 (2014).
 - [13] A. Vats, P. K. Yadav, V. Banerjee, and S. Puri, Symbiotic dynamics in living liquid crystals, *Phys. Rev. E* **108**, 024701 (2023).
 - [14] S. Zhou, O. Tovkach, D. Golovaty, A. Sokolov, I. S. Aranson, and O. D. Lavrentovich, Dynamic states of swimming bacteria in a nematic liquid crystal cell with homeotropic alignment, *New Journal of Physics* **19**, 055006 (2017).
 - [15] M. M. Genkin, A. Sokolov, O. D. Lavrentovich, and I. S. Aranson, Topological defects in a living nematic ensnare swimming bacteria, *Physical Review X* **7**, 011029 (2017).
 - [16] S. Zhou, A. Sokolov, O. D. Lavrentovich, and I. S. Aranson, Living liquid crystals, *Biophysical Journal* **106**, 420a (2014).
 - [17] P. C. Mushenheim, R. R. Trivedi, H. H. Tuson, D. B. Weibel, and N. L. Abbott, Dynamic self-assembly of motile bacteria in liquid crystals, *Soft Matter* **10**, 88 (2014).
 - [18] T. Turiv, I. Lazo, A. Brodin, B. I. Lev, V. Reiffenrath, V. G. Nazarenko, and O. D. Lavrentovich, Effect of collective molecular reorientations on brownian motion of colloids in nematic liquid crystal, *Science* **342**, 1351 (2013).
 - [19] A. Sokolov, S. Zhou, O. D. Lavrentovich, and I. S. Aranson, Individual behavior and pairwise interactions between microswimmers in anisotropic liquid, *Physical Review E* **91**, 013009 (2015).
 - [20] A. Amiri, R. Mueller, and A. Doostmohammadi, Unifying polar and nematic active matter: emergence and co-existence of half-integer and full-integer topological defects, *Journal of Physics A: Mathematical and Theoretical* **55**, 094002 (2022).
 - [21] S. Ngo, F. Ginelli, and H. Chaté, Competing ferromagnetic and nematic alignment in self-propelled polar particles, *Physical Review E* **86**, 050101 (2012).
 - [22] D. Lee and G. Grinstein, Strings in two-dimensional classical xy models, *Physical review letters* **55**, 541 (1985).
 - [23] D. Carpenter and J. Chalker, The phase diagram of a generalised xy model, *Journal of Physics: Condensed Matter* **1**, 4907 (1989).

- [24] P. S. Mondal, P. K. Mishra, and S. Mishra, Ordering kinetics and steady states of xy-model with ferromagnetic and nematic interaction, *Journal of Physics: Condensed Matter* **36**, 285101 (2024).
- [25] A. Vats, V. Banerjee, and S. Puri, Surface-directed dynamics in living liquid crystals, *Physical Review E* **110**, 034701 (2024).
- [26] F. Vafa and A. Doostmohammadi, Phase diagram, confining strings, and a new universality class in nematopolar matter, arXiv preprint arXiv:2501.04769 (2025).
- [27] I. Ruider, K. Thijssen, D. R. Vannier, V. Paloschi, A. Sciortino, A. Doostmohammadi, and A. Bausch, Topological excitations govern ordering kinetics in endothelial cell layers, *bioRxiv*, 2024 (2024).
- [28] C. Meng, J.-S. Wu, Žiga Kos, J. Dunkel, C. Nisoli, and I. I. Smalyukh, Emergent dimer-model topological order and quasi-particle excitations in liquid crystals: combinatorial vortex lattices (2025), arXiv:2502.08314 [cond-mat.soft].
- [29] A. Missaoui, K. Harth, P. Salamon, and R. Stannarius, Annihilation of point defect pairs in freely suspended liquid-crystal films, *Phys. Rev. Res.* **2**, 013080 (2020).
- [30] M. R. Nejad and J. M. Yeomans, Active extensile stress promotes 3d director orientations and flows, *Physical Review Letters* **128**, 048001 (2022).
- [31] G. Duclos, R. Adkins, D. Banerjee, M. S. Peterson, M. Varghese, I. Kolvin, A. Baskaran, R. A. Pelcovits, T. R. Powers, A. Baskaran, *et al.*, Topological structure and dynamics of three-dimensional active nematics, *Science* **367**, 1120 (2020).
- [32] J. Binysh, J. Pollard, and G. P. Alexander, Geometry of bend: singular lines and defects in twist-bend nematics, *Physical Review Letters* **125**, 047801 (2020).
- [33] J. Binysh, Ž. Kos, S. Čopar, M. Ravnik, and G. P. Alexander, Three-dimensional active defect loops, *Physical Review Letters* **124**, 088001 (2020).
- [34] G. P. Alexander, Topology in liquid crystal phases, *The role of topology in materials*, 229 (2018).
- [35] T. Machon, The topology of knots and links in nematics, *Liquid Crystals Today* **28**, 58 (2019).
- [36] O. D. Lavrentovich, Transport of particles in liquid crystals, *Soft Matter* **10**, 1264 (2014).